

Width-dependent continuous growth of atomically thin quantum nanoribbons from nanoalloy seeds in chalcogen vapor

Received: 20 May 2024

Accepted: 10 November 2024

Published online: 21 November 2024

 Check for updates

Xufan Li^{1,11}, Samuel Wyss^{2,11}, Emanuil Yanev^{3,11}, Qing-Jie Li^{4,5}, Shuang Wu¹, Yongwen Sun^{6,7}, Raymond R. Unocic^{8,9}, Joseph Stage², Matthew Strasbourg², Lucas M. Sassi^{1,10}, Yingxin Zhu^{6,7}, Ju Li^{4,5}, Yang Yang^{6,7}, James Hone³, Nicholas Borys², P. James Schuck³ & Avetik R. Harutyunyan¹✉

Nanoribbons (NRs) of atomic layer transition metal dichalcogenides (TMDs) can boost the rapidly emerging field of quantum materials owing to their width-dependent phases and electronic properties. However, the controllable downscaling of width by direct growth and the underlying mechanism remain elusive. Here, we demonstrate the vapor-liquid-solid growth of single crystal of single layer NRs of a series of TMDs (MeX_2 ; Me = Mo, W; X = S, Se) under chalcogen vapor atmosphere, seeded by pre-deposited and respective transition metal-alloyed nanoparticles that also control the NR width. We find linear dependence of growth rate on supersaturation, known as a criterion for continuous growth mechanism, which decreases with decreasing of NR width driven by the Gibbs-Thomson effect. The NRs show width-dependent photoluminescence and strain-induced quantum emission signatures with up to $\approx 90\%$ purity of single photons. We propose the path and underlying mechanism for width-controllable growth of TMD NRs for applications in quantum optoelectronics.

One-dimensional (1D) or quasi-1D electronic systems including whiskers, nanowires, and nanotubes exhibit exotic physical properties^{1–5}, which continue to fuel fundamental research and advanced applications. Recently, quasi-1D structures such as graphene nanoribbons (NRs) have been synthesized^{6–10}, showing enriched electronic structures and quantum phase tuning^{6–9} compared to graphene sheets. Theoretical calculations also predicted width-dependent crystalline phases, band structure, and spin-orbit coupling in NRs of atomically

thin two-dimensional (2D) transition metal dichalcogenides (TMDs)^{11–15}. These anticipated peculiarities have attracted broad interest in creating disruptive technologies, especially in the rapidly emerging area of 1D van der Waals (vdW) quantum materials¹⁶. To date, the dominant approach for obtaining TMD NRs with controllable widths relies on post-synthesis treatments (e.g., lithography or etching)^{17–19}. There are also reports on NR growth mediated by liquid droplets of precursors^{20,21}, or guided growth on specifically engineered

¹Honda Research Institute USA, Inc., San Jose, CA 95134, USA. ²Department of Physics, Montana State University, Bozeman, MT 59717, USA. ³Mechanical Engineering Department, Columbia University, New York, NY 10025, USA. ⁴Department of Nuclear Science and Engineering, Massachusetts Institute of Technology, Cambridge, MA 02139, USA. ⁵Department of Materials Science and Engineering, Massachusetts Institute of Technology, Cambridge, MA 02139, USA. ⁶Department of Engineering Science and Mechanics, The Pennsylvania State University, University Park, PA 16802, USA. ⁷Materials Research Institute, The Pennsylvania State University, University Park, PA 16802, USA. ⁸Center for Nanophase Materials Sciences, Oak Ridge National Laboratory, Oak Ridge, TN 37831, USA. ⁹Present address: Department of Materials Science and Engineering, North Carolina State University, Raleigh, NC 27695, USA. ¹⁰Present address: Department of Physics, National University of Singapore, Singapore 117551, Singapore. ¹¹These authors contributed equally: Xufan Li, Samuel Wyss, Emanuil Yanev. ✉e-mail: aharutyunyan@honda-ri.com

substrates through aligned steps^{22–24} or chemical treatment²⁵ to realize aligned NRs with even controllable edge structures²⁴. However, the results widths were generally >50 nm and still lack of control on the width. Recently, we reported a direct synthesis of bilayer MoS₂ NRs with width down to sub-10 nm after a mild treatment¹⁸. Nevertheless, interference with intrinsic properties by post-synthesis treatments and lack of effective control on NRs width during growth made it difficult to study their pristine width-confined properties, thereby hindering their potential applications. On the other hand, deeper understanding of NR growth mechanism could not only guide the direct width-controlled growth but also enrich the fundamental science as an example of formation of 1D or quasi-1D nanocrystals.

Among various established methods, chemical vapor deposition (CVD) has been widely used to synthesize various 1D or quasi-1D nanostructures in a broad diameter range^{26–28}, from which many peculiarities of growth mechanisms have been revealed since its first exploitation in the 1960s in the growth of Si whiskers^{29–35}. Indeed, through classical analysis on the experimental finding that narrower whiskers grew more slowly, Givargizov³⁰ derived an empirical model predicting quadratic growth rate dependence on reciprocal of the diameter of Au-catalyzed Si whiskers with a critical diameter (≤ 50 nm), below which the whisker cannot grow. This diameter-dependence and limit was explained by Gibbs-Thomson effect, i.e., the supersaturation of silicon in Au-Si droplet decreases with the droplet size. However, although such a model was later confirmed by many studies on the growth of other semiconducting nanowires^{29,33}, there were reports showing diameter-independent growth rate, explained by irreversible catalytic dissociation of exploited Si precursor³⁴. Moreover, there also have been reports showing the opposite growth rate-diameter relation where narrower nanowires grew faster due to adatom diffusion on the nanowire surface^{31,32}. However, the growth mechanism of atomically thin 1D NRs has barely been studied.

In this work, we present a CVD growth of single layer (SL) TMD NRs mediated by seed nanoparticles (NPs) in chalcogen vapor atmosphere. The seed NPs are based on nanoalloys of metal precursor and catalyst (i.e., Mo-Ni or W-Mg), which also control the width of the grown NR. Based on the length vs. width analysis of grown SL MoS₂ NRs under different vapor supersaturation, we discover that unlike previously studied 1-D structures, i.e., whiskers and nanowires, the growth rate of NRs is a linear function of supersaturation, decreasing linearly with the reciprocal of width controlled by the Gibbs-Thomson effect, which is characteristic of continuous growth. As an example of exploiting the quantum nature of the NRs, we demonstrate deterministic quantum emission (QE) signatures induced by localized strain, making them promising candidates as single photon sources for quantum communications.

Results

Growth of Single Layer MoS₂ NRs

Synthetic fluorophlogopite mica (F-mica) with (001) surface plane was used as the substrate, which has been used for vdW epitaxial growth of 2D flakes before³⁶. Unlike typical one-step synthesis^{18,20,21,37}, we used a two-step growth approach: First formation of partial precursor/seed NPs followed by introduction of corresponding chalcogen vapor. Specifically taking MoS₂ as an example, we first deposited NPs on the substrate by evaporating a mixture of MoO₃, Ni, and NaBr powder under a moisturized Ar flow in a tube furnace system (Fig. 1a, step 1; Fig. 1b). The presence of NaBr enabled co-deposition of Ni and MoO₃. The deposited NPs are composed of Na-Mo-Ni-O (Fig. 2a, b), in which the Mo atomic ratio within (Mo-Ni) varies in a broad range of $\approx 10\%$ –85%. It is important to note that the presence of moisture was essential for the formation of the Na-Mo-Ni-O compound from the precursor powder mixture; without moisture, only NaBr was deposited on the substrate (Supplementary Fig. 1a–c)¹⁸. The NPs were then exposed in a sulfur vapor atmosphere, generated by heating sulfur powder, in a

separate tube reactor (Fig. 1a, step 2), resulting in “tip”-growth of MoS₂ NRs from the NPs, with widths comparable to the tip-NP (inset of Fig. 1c, Supplementary Fig. 2a, b) and lengths from a few to tens of micrometers (Fig. 1c, Supplementary Fig. 1). Despite the reduction of seed NPs’ diameter during the NR growth (Supplementary Fig. 3), their diameter distribution correlates with that of NR width (Supplementary Fig. 2c), which allows control of width distribution of NRs through controlling the diameter distribution of pre-deposited seed NPs. It is also noted that in some areas the as-grown NRs show a certain extent of alignment (i.e., Fig. 1c) while in others they do not, which could be related to the specific surface condition and crystallographic orientations of the F-mica substrate.

Atomic force microscopy (AFM) analysis (Fig. 1d, Supplementary Fig. 2e) and Raman spectroscopy (Fig. 1e, Supplementary Fig. 4) confirm the SL MoS₂ NRs. Scanning transmission electron microscopy (STEM) with fast Fourier transform (FFT) analysis indicates that the NR is single crystal, with the axial growth along the [010] direction (Fig. 1f). Occasionally single crystal NR grown along the [110] direction was also observed (Supplementary Fig. 5). Atomic-resolution high-angle annular dark-field STEM (HAADF-STEM) shows clean, well-defined honeycomb lattice with a lattice parameter $a \approx 0.308$ nm of MoS₂ NRs, which is terminated by zigzag edge structures (Fig. 1g, Supplementary Fig. 5d, e). Detailed Auger electron spectroscopy (AES) analysis (Fig. 2a–c, Supplementary Fig. 6) and HAADF-STEM combined with FFT analysis (Fig. 2d–g) reveal that during NR growth the composition of seed NP evolved from Na-Mo-Ni-O (Fig. 2a, b) to a pure Ni NP with a face-centered cubic (fcc) structure (Fig. 2e, f), as a result of consumption of Mo atoms in the seed NP by MoS₂ NR through precipitation under S vapor atmosphere. The precipitation in turn drives the motion of NP along the axial growth direction of NR (see Supplementary Fig. 7 showing no motion of NP without precipitation). As the growth temperature in step 2 is above the liquefaction temperature of the seed NP (≈ 725 °C)¹⁸, the growth follows a VLS mechanism. It should also be noted that Na and Ni were not detected from the NR in AES measurement (Fig. 2c, Supplementary Fig. 6), indicating that the as-grown NRs are purely MoS₂. The electrical properties of the SL MoS₂ NR at room temperature show typical n-type behavior with an on/off ratio of $\approx 10^6$ (Supplementary Fig. 8) and a current density comparable to the best CVD-grown MoS₂ reported with various contacts^{38,39}.

Growth mechanism of MoS₂ NRs

To understand the S-driven precipitation of MoS₂ on the atomic level and the role of multiple constituents in the seed NP, we performed molecular dynamics (MD) simulation (Fig. 2h). For an initially equilibrated Na-Mo-Ni-O NP at 650 K with S atoms, shows formation of triangular Mo-S local structural motifs bonded by Ni atoms, which could be the basic building blocks of MoS₂ NRs (Fig. 2i). Ni atoms also play a role in connecting different triangular units together (Fig. 2j). Those Mo-S motifs form even larger two-dimensional Mo-S structures as S continues to react with the system (Fig. 2k). It is noted that the oxygen in the system also plays an important role for the separation of Ni-MoS₂. In contrast to the equilibrated Na-Mo-Ni-O system with a relatively uniform distribution of all constituting elements (Supplementary Fig. 9b), the system without O (Na-Mo-Ni) evolves to a core-shell structure with Na atoms on the surface and a mixture of Ni and Mo in the interior of the nanoparticle (Supplementary Fig. 9c). Such a system keeps a core-shell structure after equilibrated with S atoms, only with slight mixing of Ni atoms with surface Na atoms (Supplementary Fig. 9a).

Next, we studied seed NP-mediated growth mechanism of SL MoS₂ NRs. As mentioned above, investigation on the relation of length (L) vs. diameter (d) of catalytic NP could provide specific insights on VLS growth mechanism of various 1D nanostructures. Therefore, we carefully analyzed our NR L vs. width (W) relationship grown at the same temperature ($T = 730$ °C) for a fixed growth duration $t = 180$ s.

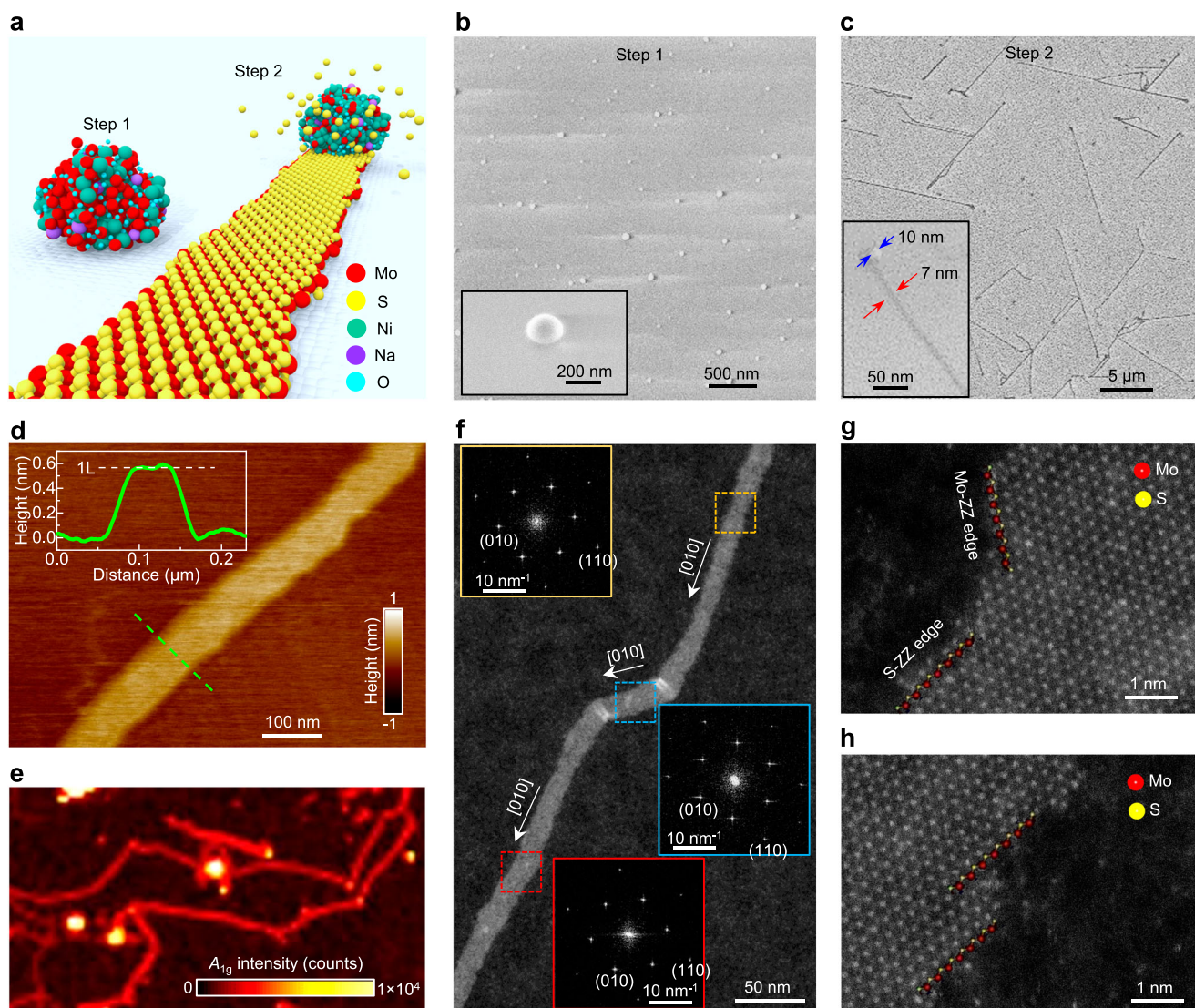


Fig. 1 | SL MoS₂ NRs grown on F-mica substrate. **a** Illustration of the two-step growth of SL MoS₂ NRs on F-mica substrate. Step 1: Seed NPs deposition. Step 2: Sulfurization of seed NPs resulting in precipitation of MoS₂ NR. Color code of the atoms: Mo (red), S (yellow), Ni (green), Na (purple), O (blue). **b** SEM image of Na-Mo-Ni-O seed NPs deposited for 1 min. Inset is the enlarged view of a NP. **c** SEM image of resulting MoS₂ NRs. Inset is the enlarged view of a NR width of ≈ 7 nm, comparable to the diameter of the tip Ni NP. **d** AFM image and height profile confirming the SL NR. **e** Raman intensity mapping of the A_{1g} peak of the SL MoS₂ NRs grown on F-mica. The color scales in **(d, e)** are linear. **f** Low-magnification HAADF-STEM image showing a length of ≈ 500 nm of a SL MoS₂ NR with two kinks. Insets with yellow, blue, and red borderlines are FFT patterns acquired from three

different regions indicated by the dashed yellow, blue, and red boxes, respectively, indicating the growth axis of NR along the [010] crystal direction. The good alignment between the NR and diffraction pattern orientation, even in the kinked region (blue box), indicates the NR is single crystal. The kinks are used for strain analyses shown in Supplementary Fig. 19. **g, h** Atomic-resolution HAADF-STEM images showing edge structures of the upper side of the NR in the yellow box and lower side in red box, respectively, in **(f)**. Although the FFT patterns and atomic resolution lattice show the edge is along the (110) plane, i.e., armchair, they are mostly terminated by zigzag structures resulting in steps. Source data are provided as a Source Data file.

Statistics on measured L and W of individual NRs grown under different sulfur vapor pressures (P_{sulfur}) (Supplementary Fig. 10) based on the SEM images (typical results shown in Supplementary Fig. 11) show a general trend that wider NRs grow longer than shorter ones (Fig. 3a). Since the NRs in general kept growing for $t > 180$ s (Supplementary Fig. 12), we assume the growth rate $V_g = L/t$ (when $t \leq 180$ s), which means that wider NRs grow faster than narrower ones. It is also obvious in Fig. 3a that V_g increases with increasing P_{sulfur} , and the overall width distribution shifts to smaller width as P_{sulfur} increases (Fig. 3b), indicating that the smallest width of NR decreases with increasing supersaturation, i.e., shifting from 60–70 nm to 7–10 nm as P_{sulfur} increasing from 7.6×10^{-5} atm to 0.017 atm (see Suppl. Note 1 for more detailed discussion on width distribution).

In crystal growth theory, the growth rate can be described by $V_g = K_g(\Delta\mu/(k_B T))^n$, where K_g is the kinetic factor, $\Delta\mu$ the difference of chemical potentials, k_B the Boltzmann constant, T is the temperature, and n is the order (typically $n=1$ or 2, corresponding to linear or quadratic growth of nanowires³⁰). We consider the following steps for NR growth: i) impingement of S atoms into the liquid Na-Mo-Ni-O droplet from vapor phase due to difference in chemical potentials of S on vapor-liquid boundary, $\Delta\mu_{\text{vl}}$, which depends on the droplet diameter, ii) formation of Mo-S motifs and diffusion towards droplet-substrate boundary, and iii) crystallization of the liquid alloy on the substrate under the droplet by precipitation of Mo-S motifs due to chemical potentials difference $\Delta\mu_{\text{ls}}$ between the liquid droplet and solid MoS₂ NR, which also depends on droplet diameter. Unlike most

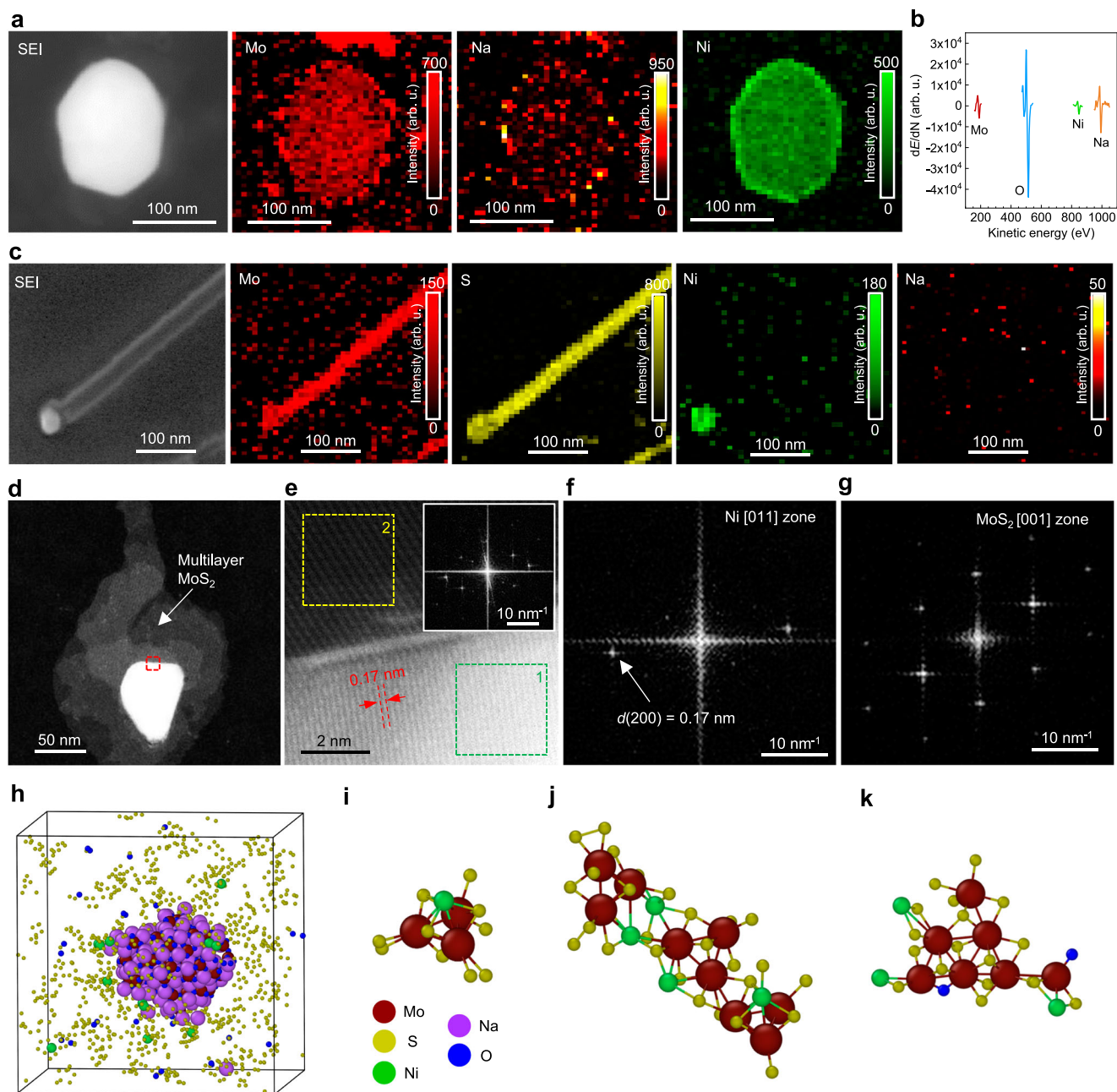


Fig. 2 | Evolution of seed NPs. a AES elemental mapping of Mo, Na, and Ni in a seed NP. SEI stands for secondary electron image. **b** Corresponding AES spectra of Mo (red), Na (orange), Ni (green), and O (blue) in the NP. Note that AES analysis the NPs were deposited on a SiO₂/Si substrate. **c** AES elemental mapping of Mo, S, Ni, and Na of a SL MoS₂ NR including the tip NP, transferred on a SiO₂/Si substrate after growth. The Mo and S signal at the NP tip area come from the multilayers of MoS₂ precipitated from the tip NP during the cooling down (see **d**). The color scales in (**a**) and (**c**) are linear. **d** Low-magnification STEM image of a MoS₂ NR emanating from the NP tip. **e** High resolution HAADF-STEM image of the region indicated by the dashed red box in (**d**), showing the interface between the tip NP and MoS₂. Inset is

the FFT pattern of the whole image. **f, g** FFT pattern acquired from the dashed green box 1 and dashed yellow box 2 in (**e**), showing Ni [011] zone and MoS₂ [001] zone, respectively. **h** MD simulation of a Na-Mo-Ni-O NP interactions with S atoms, showing separation of Ni atoms from the other nanoparticles atoms after being equilibrated at 650 K for 6 ns. Color code of the atoms: Mo (dark red), S (yellow), Ni (green), Na (purple), O (blue). **i-k** Extended simulation of the Na-Mo-Ni-O NP in the S environment for 10 ns at 525 K, showing that Mo atoms in the NP start to form triangular local structural motifs with a Ni atom on the top (**i**), inter-connected triangular Mo local motifs (**j**), and embryo of two-dimensional hexagonal structures (**k**) Source data are provided as a Source Data file.

of the typical nanowire and SL TMD growth, there is no growth through the vapor-solid interface by direct incorporation of S atoms from vapor into the solid MoS₂ NR via terrace/edge impingement since there is no Mo vapor in the surrounding atmosphere. Hence, the only driving force for NR growth is the supersaturation of Mo-S motifs concentration in the droplet relative to solid NR, which elevates due to the impinging of S atoms from vapor phase into droplet. Considering S

vapor as an ideal gas, the supersaturation of S atoms in the droplet with diameter (d) according to Gibbs-Thomson effect³⁰ could be expressed as

$$\Delta\mu_{v1}/(k_B T) = \Delta\mu_{\infty}/(k_B T) - 2\sigma_{v1}\Omega/(dk_B T) \quad (1)$$

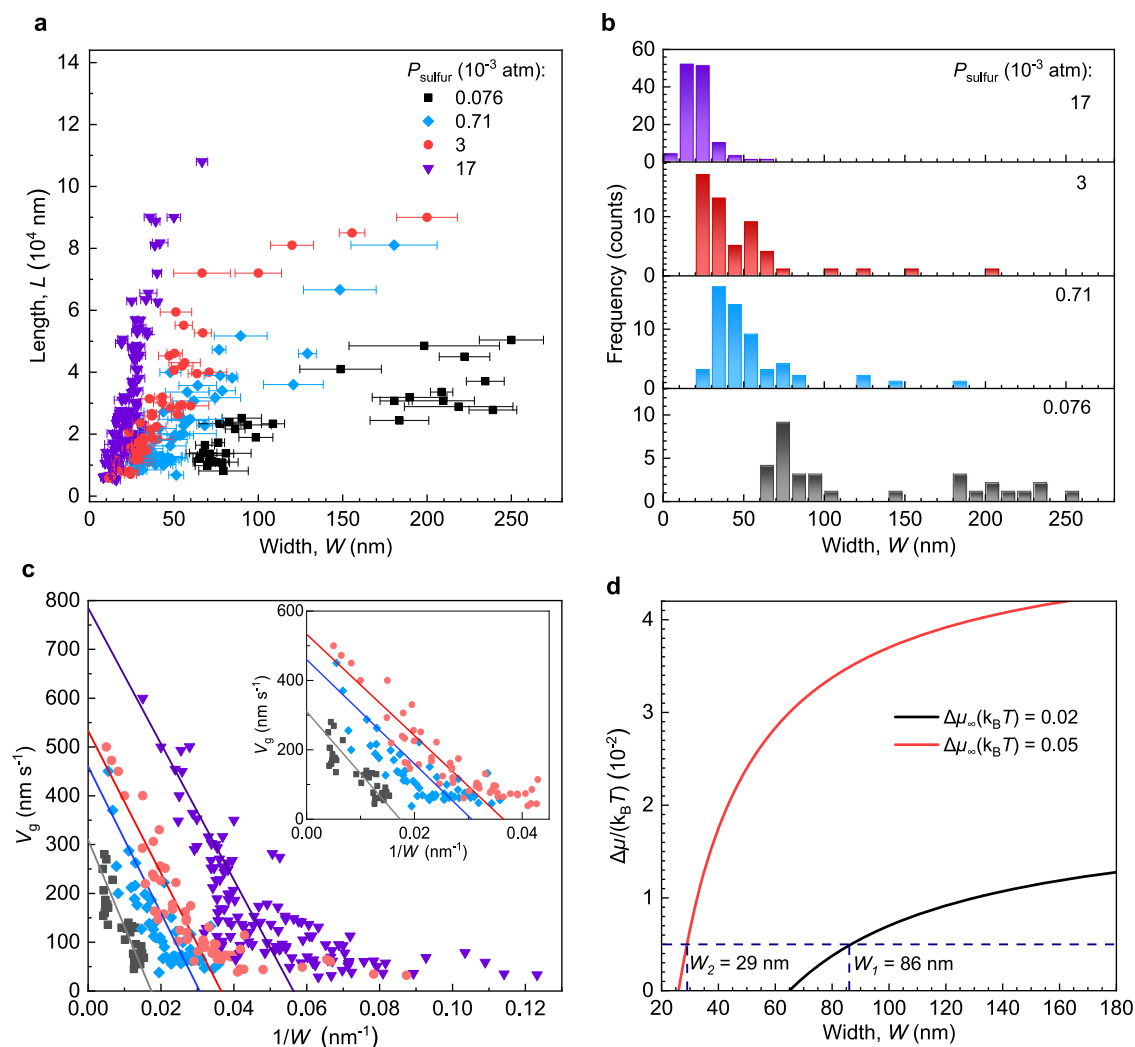


Fig. 3 | Precipitation-driven growth mechanism study. **a** Statistics of dependence of NR L on W with $T_{\text{sulfur}} = 130, 170, 200,$ and 250 °C, corresponding to $P_{\text{sulfur}} = 7.6 \times 10^{-5}$ (black symbols), 7.1×10^{-4} (blue symbols), 0.003 (red symbols), and 0.017 atm (purple symbols), respectively. The NRs were grown for 180 s. The L vs W data of the NRs have been collected from three independent growth experiments at a given growth temperature (730 °C) for each P_{sulfur} (T_{sulfur}). The error bars represent the variations of width along the length of each NRs. **b** Histograms of

width distribution of MoS_2 NR measured in **(a)**, with $P_{\text{sulfur}} = 7.6 \times 10^{-5}$ (black), 7.1×10^{-4} (blue), 0.003 (red), and 0.017 atm (purple). **c** Growth rate V_g vs. $1/W$ with different P_{sulfur} . The color code corresponds to **(a)**. Solid lines are fitting results using Eq. (2) with $n=1$. Inset is enlarged view of $P_{\text{sulfur}} = 7.6 \times 10^{-5}$, 7.1×10^{-4} , and 0.003 atm. **d** Actual supersaturation $\Delta\mu_{\text{v,l}}/(k_B T)$ vs. W according to Eq. (1) with $\Delta\mu_{\infty}/(k_B T) = 0.02$ (black curve) and 0.05 (red curve), corresponding to $P_{\text{sulfur}} = 7.6 \times 10^{-5}$ and 0.003 atm. Source data are provided as a Source Data file.

where $\Delta\mu_{\infty}/(k_B T) = \ln(P_{\text{sulfur}}/P_{\infty})$ is the supersaturation between vapor and the droplet with infinite interface, P_{∞} is the pressure on the infinite boundary of S and droplet, σ_{vl} the surface energy of Ni-Mo alloy ($\approx 1.7 \text{ J m}^{-2}$), Ω is the S atomic volume in the droplet (0.0056 nm^3), $k_B = 1.380649 \times 10^{-23} \text{ J K}^{-1}$, and $T = 1003 \text{ K}$ is the synthesis temperature (see Suppl. Note 2 for detailed explanation). Correspondingly, V_g could be expressed as

$$V_g = K_g (\Delta\mu_{\infty}/(k_B T) - 2\sigma_{\text{vl}}\Omega/(dk_B T))^n \quad (2)$$

Furthermore, we found that the width of grown NRs is related to the diameter of the droplets by $d = W/(\sin\alpha) \approx W/0.75$, based on experimental observations of contact angle between NP droplet and the NR (Supplementary Fig. 2b). Hence, we analyzed the plots of V_g vs. $1/W$ for NRs grown under different P_{sulfur} (Fig. 3c). In the lower supersaturation region (i.e., larger W or d), V_g decreases linearly with increasing $1/W$, and each plot could be best fitted using Eq. (2) with $n=1$, from which nearly constant K_g values for all P_{sulfur} were extracted (Table 1). However, it should be noticed that as supersaturation gets

Table 1 | Kinetic factor (K_g), critical width (W_c) of NRs, and supersaturations at infinite boundary ($\Delta\mu_{\infty}/(k_B T)$) under different sulfur vapor pressure (P_{sulfur})

P_{sulfur} (atm) / T_{sulfur} (K)	K_g (10^{-5} m s^{-1})	W_c (nm)	$\Delta\mu_{\infty}/(k_B T)$ ($T = 1003 \text{ K}$)
6×10^{-5} / 403	1.15	56	0.02
1×10^{-4} / 443	1.09	33	0.04
3×10^{-3} / 473	1.06	26	0.05
1.7×10^{-2} / 523	1.01	17	0.08

higher, especially for $W < 20 \text{ nm}$, V_g becomes almost independent of $1/W$. Such a behavior is more dominant as P_{sulfur} gets higher (e.g., $P_{\text{sulfur}} = 0.017 \text{ atm}$), which results in NRs with mostly narrower widths (Fig. 3c). Such a deviation from the Gibbs-Thomson effect could be attributed to the peculiarities of our NR formation. Specifically, in our method the seed droplet is the only source for Mo atoms, whose solubility in the Ni-Mo-O nanoalloy generally depends on the droplet size when $d < 20 \text{ nm}$, which affects the supersaturation of Mo-S motifs

in the droplet and thereby on the growth rate. The reduction of the solubility of Mo in the droplet with decrease of droplet size can drive excess precipitation, resulting in increase of the growth rate⁴⁰. Due to the lack of data for this quaternary nanoalloy phase diagram, further study is needed on this scope.

To further validate the growth mechanism of single-crystal SL MoS₂ NRs, as shown in the structural analysis (Fig. 1f, g), we analyzed the growth rate of NRs with different width but grown under the same supersaturation on the vapor-liquid interface. The interceptions of the fitting lines for V_g vs. $1/W$ with the $1/W$ -axis in Fig. 3c, where growth rate is zero, provide critical widths $W_c = 2\alpha_{vl}\Omega/\Delta\mu_{\infty}$ under different P_{surf} according to Gibbs-Thomson model. For given values of W_c , we obtained the corresponding values of supersaturation $\Delta\mu_{\infty}/(k_B T)$ for different P_{surf} from Eq. (2) (Table 1). Using Eq. (1), the width dependence of actual supersaturation $\Delta\mu_{vl}/(k_B T)$ for $\Delta\mu_{\infty}/(k_B T) = 0.02$ and 0.05 were plotted (Fig. 3d), from which we found two width values $W = 86$ and 27 nm, with a same actual supersaturation, i.e., $\Delta\mu_{vl}/(k_B T) = 0.005$. They correspond to growth rate $V_g = 80$ and 25 nm s⁻¹, respectively, according to V_g vs. $1/W$ experimental graph in Fig. 3c. The results indicate that even though the interface area under the droplet of the wider NR (≈ 7400 nm²) is about 10 times larger than that of the narrower one (≈ 730 nm²), the V_g is only ≈ 3 times higher, which excludes the monocentric nucleation-mediated growth that could result in observed single crystal NRs. As shown above the growth rate, $V_g = K_g(\Delta\mu/(k_B T))$, depends linearly on $\Delta\mu$ with nearly constant kinetic factor K_g for all P_{surf} (Fig. 3c and Table 1), i.e. within the experimental range of applied supersaturations ($\Delta\mu < 0.25k_B T$) K_g can be considered independent of $\Delta\mu$. The linear dependence of V_g on $\Delta\mu$, as an experimental criterion, suggests that the formation of single crystal NR is the result of a continuous growth⁴¹ through the attachment of atoms from the supersaturated droplet alloy to the NR edges with atomic steps/kinks as growth sites of the SL MoS₂ nucleus that grows axially under the droplet.

Growth of other TMD NRs

Beyond MoS₂, we used the two-step method above to grow other SL TMD NRs including MoSe₂, WS₂, and WSe₂ on F-mica substrates. MoSe₂ NRs were also precipitated from pre-deposited Na-Mo-Ni-O seed NPs, driven by selenium vapor (Supplementary Fig. 13). However, W-based TMD NRs are grown from pre-deposited seed NPs composed of Na-W-Mg-O, in which Mg plays a similar role as Ni (Supplementary Figs. 14–16), which points out the importance of nanoalloy composition.

Width-dependent optical properties of NRs

Next, we attempted to reveal whether the width as an additional degree of freedom enabled by NR geometry could endow tunable intrinsic properties of NRs. We found that the optical properties of NRs are influenced by their width. Specifically, at room temperature, the SL MoS₂ NRs show width-dependent photoluminescence (PL) from the A-exciton (Fig. 4a), which is further corroborated on the nanoscale with nano-PL characterization of individual NRs using tip-enhanced PL (TEPL) measurement. (Supplementary Fig. 17). The PL of the A-exciton blueshifts as the width of the NR decreases, similar to the trend observed in ref. 25. The microscopic origins of such width-dependent PL of the NRs could arise to an interplay between interior states and edge states. The energy blueshift is most pronounced in the range of 50–20 nm, where a linear dependence on $1/W^2$ is shown (inset of Supplementary Fig. 17c), indicating that the energy shift is due to the weak confinement on exciton center-of-mass in an infinite potential well^{42–44}; while for NRs with width > 50 nm, the energy shift could be dominant by the edge states, where strain relaxation, chemical termination, and/or interaction with the substrate result in localized states as previously reported in nearfield studies of 2D crystallites^{45,46}. Preliminary measurements show that such edge states may also exist

in the MoS₂ NRs (Supplementary Fig. 18), and future measurements will focus on unraveling how these states contribute to the width-dependent effects observed here.

Quantum emission from strain-engineered TMD NRs

Further, strain engineering has been widely used for tailoring excitonic light-matter interactions and deterministically creating localized electronic states in 2D semiconductors^{47–51} for potential applications. For our SL NR systems, analysis of atomic resolution HAADF-STEM imaging (Supplementary Fig. 19) reveals that they can accommodate from -14% (compressive) to +14% (tensile) strains. Optically, the SL TMD NRs preserve the strain-tunable intense excitonic light-matter interactions that are expected from SL 2D semiconductors⁵². Exploiting the observed mechanical robustness, we transferred as grown SL MoS₂ and WSe₂ NRs onto arrays of gold nanocones (inset of Fig. 4b)^{49,50} to realize strain-induced localized states. The gold nanocones have an average height and base diameter of ≈ 100 nm, and a radius of curvature at the apex of ≈ 5 nm (Supplementary Fig. 20). For a SL MoS₂ NR with a width of 100 nm, the strain induced by being draped over the gold nanocone (Fig. 4b, red curve) generates a pronounced localized exciton state at 1.77 eV that is $\approx 2 \times$ brighter with a narrower linewidth (≈ 25 meV) than the PL of the free A exciton at 1.97 eV. In contrast, such a strong feature is absent in the PL spectrum acquired from the unstrained NR (Fig. 4b, blue curve). Similar strain-localization of excitons at the same energy (1.77 eV) in SL MoS₂ NRs are observed at room temperature in nanoscale regions directly surrounding a NR draped over a nanocone by nano-PL imaging (Supplementary Fig. 21). In the time evolution of the PL spectra from the strained region (inset of Fig. 4b), the PL intensity and energy of the A exciton 1.97 eV does not show any temporal variation, which is expected for a state that is not localized; in contrast, emission from the strained region exhibits spectral wandering (i.e., random jumps to different energies) and intensity fluctuations on the timescale of seconds, which are both signatures of highly localized quantum dot-like states that can generate single photons⁴⁸. This report introduces purely strain-induced quantum dot-like states in single-layer MoS₂ without the use of ion irradiation⁵³ (see Suppl. Note 3 for more detailed discussion).

Finally, using the same strain-engineering method on SL WSe₂ NRs, we confirm the ability to fabricate single photon emitters (SPEs) in the more confined geometry of the NRs. Figure 4c shows that bright, narrowband emitters emerge from localized strained regions of a ≈ 100 nm-wide SL WSe₂ NR that is draped over a similar array of gold nanocones (Supplementary Fig. 22a). Nano-PL imaging (inset of Fig. 4c, Supplementary Fig. 22b) reveals a series of bright emissive spots that each correspond to a region where the SL WSe₂ NR is draped over an individual cone. The selected spectrum in Fig. 4c is from the cone site that is marked in the inset. Similar spectra are observed from the other cone-induced strained sites, with emitter energies ranging from 1.6–1.7 eV (Supplementary Fig. 22b, c; 40–50 meV lower than the free exciton in unstrained WSe₂ at 4 K). The linewidths of the strain-induced emitters are $> 10 \times$ narrower, and their intensities are 100–1000 \times brighter than the localized state in the SL MoS₂ NR (Fig. 4b). The much larger intensity of these emitters permits measurement of the second-order autocorrelation function $g^{(2)}(\tau)$ using a Hanbury-Brown-Twiss interferometer (see Methods), which reveals clear photon antibunching with a purity of 80%–90% (Fig. 4d, Supplementary Fig. 23). The demonstration of antibunching in a TMD NR system sets the stage for further research into the width-dependent optical properties of the NRs (i.e., Fig. 4a) and the use of local strain engineering, specific to the NR geometry, to potentially create more homogenous populations of 2D semiconductor-based SPEs for broadscale quantum photonic applications.

In conclusion, we developed a facile method for direct growth of single-crystal SL TMD NRs, which allows controllable downscaling NRs widths down to 7 nm. Deconvolution of seed NP formation and NR

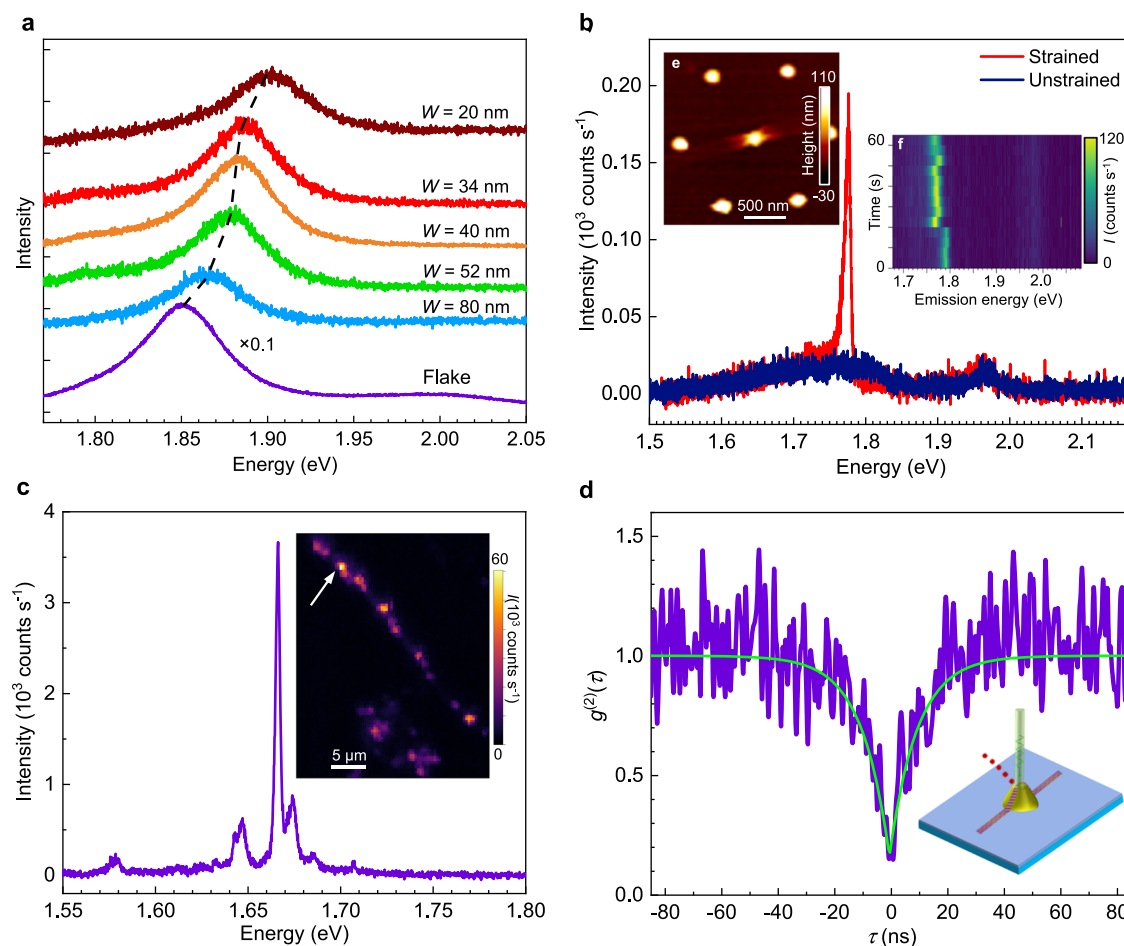


Fig. 4 | Width-dependent PL and quantum light emission from strained SL MoS₂ and WSe₂ NRs. **a** PL spectra of SL MoS₂ flake (purple curve) and NRs with width of 80 (blue curve), 52 (green curve), 40 (orange curve), 34 (red curve), and 20 nm (dark red curve) at room temperature. **(b)** PL spectra of a MoS₂ NR draped over an Au nanocone, from the region over the cone (strained, red curve) and unstrained region (dark blue curve) at $T = 4$ K. Inset **(e)**: AFM topography of the SL MoS₂ NR draped over a cone. Inset **(f)**: time-series of the PL spectra from strained region. **c** PL

spectrum of one of the strained regions (indicated by the white arrow in the inset) of a SL WSe₂ NR on Au nanocones (see Supplementary Fig. 20) at $T = 4$ K. Inset: Mapping of integrated PL intensity from the WSe₂ NR. The color scales in **(b)** and **(c)** are linear. **d** $g^{(2)}(\tau)$ measurement of the emitter in **(c)** at 1.67 eV. The fitting of the $g^{(2)}(\tau)$ curve (green curve)⁶⁰ gives a single photon purity of 81%. Inset is the illustration of quantum light emission generated from strain-engineering NRs by nanocones. Source data are provided as a Source Data file.

growth process allows independent control over the width of the NRs via diameter of seed NPs. Unlike other 1D nanostructures such as whiskers and nanowires, we reveal a continuous growth mechanism for NRs with the growth rate that depends linearly on the reciprocal width of NRs due to the Gibbs-Thomson effect. The NRs show significant mechanical robustness that can accommodate up to $\approx 14\%$ compression and tensile strain. The strain-induced localized quantum dot like states emit single photons in TMD NRs. The initial results on the SL WSe₂ nanoribbons demonstrate the great potential to realize precisely localized quantum light sources in NRs of TMDs for quantum optoelectronic applications.

Methods

Material synthesis

SL MoS₂ NRs were synthesized in a tube furnace system similar to ref. 18. Specifically, two separate argon gas lines are connected to the tube furnace, in which one directly goes to the reaction chamber (called F_{Ar}) while the other goes through a small bubbler, containing 2 mL of DI water to produce moisturized Ar (called F_{Ar/H₂O}) before reaching the reaction tube, resulting in a moisturized Ar flow with ≈ 3000 ppm H₂O. In the first step, a mixture of MoO₃, NaBr, and Ni powder at a certain weight ratio was placed in an alumina boat, and a

piece of freshly cleaved F-mica was placed ≈ 3 mm above the precursor. The precursor was heated to 730 °C under a gas flow of 40 cm³ STP min⁻¹ of F_{Ar} combined with 40 cm³ STP min⁻¹ of F_{Ar/H₂O} to allow seed NPs deposited on the F-mica. In the second step, the F-mica with deposited seed NPs was placed in another clean alumina boat and heated to 730–770 °C at the center of the tube furnace, and meanwhile, sulfur powder, placed at the upper stream, was heated separately by a heating belt to 130–270 °C to provide sulfur vapor, carried by a dry Ar flow of 80 cm³ STP min⁻¹ to sulfurize seed NPs. For the growth of MoSe₂ NRs, the same seed NPs were used, while selenium powders were heated to 350–420 °C to provide selenium vapor carried by a combination of 80 cm³ STP min⁻¹ Ar and 6 cm³ STP min⁻¹ H₂. For the growth of WS₂ and WSe₂ NRs, seed NPs were deposited from a mixture of WO₃, NaBr, and Mg precursor.

Characterization

The as-synthesized MoS₂ NRs were characterized using scanning electron microscopy (SEM, FEI QUANTA FEG 650, operating at 5 kV), atomic force microscopy (AFM, Bruker Dimension Icon), Raman spectroscopy (Renishaw inVia Raman microscope, with 1800 grooves mm⁻¹ grating and a 532 nm laser, 1 mW laser power, as excitation source). AES was conducted in a PHI 700 scanning Auger nanoprobe

(Physical Electronics) at a working voltage and current of 10 kV and 10 nA. The samples for TEM and STEM characterization were prepared using a wet transfer process. Poly(methyl methacrylate) (PMMA) 495A4 (MicroChem) is first spun onto the F-mica substrate with monolayer crystals at 3500 rounds min^{-1} for 60 s. The PMMA-coated substrate was then floated on deionized (DI) water to detach the PMMA film with the ribbons from the substrate. The floating PMMA film was scooped onto a 3 nm-thick amorphous carbon film supported by a Au TEM grid, which was subsequently soaked in acetone for 12 h to remove PMMA and get a clean sample surface. The transferred samples were finally annealed at 200 °C in vacuum to get rid of the solvent. STEM images were acquired at 60 kV using a Nion UltraSTEM equipped with a probe aberration corrector (the convergence angle was 31 mrad). The inner and outer collection angle of the HAADF detector were 86 and 200 mrad, respectively. To enhance the signal-to-noise ratio, atomic-resolution STEM images were blurred using a 2D Gaussian distribution.

Device fabrication

The FET devices were fabricated using electron-beam (e-beam) lithography patterning, performed by Nanobeam n64 Electron Beam Writer system. The electron beam was operated at an accelerating voltage of 80 kV. Metal electrodes of Bi/Au (20 nm/40 nm) were deposited on top of MoS₂ NRs in Angstrom EvoVac Deposition system, the deposition vacuum level is $<5 \times 10^{-7}$ Torr. Transport measurements were performed in a CTI-Cryogenics Model 22 Refrigerator using a Keysight B1500A Semiconductor Device Parameter Analyzer.

MD simulations

MD simulations were carried out using LAMMPS⁵⁴, with a recent universal neural network interatomic potential called PFP as implemented on the Matlantis™ platform⁵⁵. PFP has been demonstrated with DFT-level accuracy and has been successfully applied in modeling a wide range of materials. Our MD simulations employed the v4.0.0 version of PFP with the “CRYSTAL_U0” mode. The initial structures of nanoparticles were prepared using the packmol software⁵⁶. Nanoparticle with oxygen contains 500 atoms, with 143 Na atoms, 57 Mo atoms, 14 Ni atoms and 286 Oxygen atoms. Nanoparticle without oxygen contains 133 Na atoms, 33 Mo atoms, and 13 Ni atoms. The initial configuration was equilibrated at 300 K for 1 ns, using constant temperature, constant volume MD simulations (NVT), with sufficient vacuum regions (at least >24 Å, the effective interaction range from the graph convolution operations) to avoid image interactions. S atoms were randomly inserted into the simulation box to observe their interactions with nanoparticles. All subsequent simulations at different temperatures were carried out under NVT conditions. Structures were visualized using the Ovito software⁵⁷.

Strain analysis

First, we performed filtering to improve the signal-to-noise ratio in the atomic resolution STEM images. Fast Fourier transformation (FFT) has been performed on the red boxes in Supplementary Fig. 19c, d. Reciprocal space around the first-order Bragg peaks is chosen to conduct the inverse FFT, which effectively enhances the contrast of atomic columns and facilitates further detection. The second step is to locate the positions of all the atomic columns that are of interest in the filtered HAADF-STEM images, as shown in Supplementary Fig. 19e, f. The peak finding algorithm offered by the ATOMAP Python library⁵⁸ is leveraged to identify initial atomic positions, with the relative intensity threshold and minimum peak separation serving as inputs. The initial positions are further refined, first by determining the center-of-mass and then by two-dimensional (2D) Gaussian peak fitting. This allows for a precise determination of the 2D atomic column positions. Third, two sets of non-parallel planes are selected to measure the relative variations in plane distance compared to the reference value obtained away from the MoS₂

kinks at the middle section in Supplementary Fig. 19b. Previously, the TopoTEM Python library⁵⁹ has been employed for strain calculation via interplanar distance variation with the reference value in HAADF-STEM images for crystal with orthogonal axes. Building upon this, we perform a detailed basis vector transformation from inter-planar direction to orthogonal basis in MoS₂ strain study. This enables the computation of MoS₂ displacement field on an orthogonal basis, which subsequently leads to the calculation of in-plane hydrostatic strain mapping results, as shown in Supplementary Fig. 19g, h. The in-plane hydrostatic strain variation along the lines depicted in Supplementary Fig. 19e, f has been calculated. The average value is plotted along the diagonal direction, which reveals a higher magnitude of hydrostatic strain closer to the MoS₂ kinks, as shown in Supplementary Fig. 19i.

Nanocone fabrication

Substrates with nanocone stressor arrays were fabricated according to the process outlined by Yanev et al.⁵⁰. A base layer of gold was evaporated onto a silicon wafer, followed by electron-beam lithography and Al₂O₃ deposition. After lift-off, disks of alumina were left behind, which served as a hard mask during the final argon ion milling step. See ref. 44 for more details and discussion of the fabrication process.

NR transfer on nanocones

A piece of polydimethylsiloxane (PDMS) film (1 × 1 cm², Gel-Pek) is first stamped onto the as-grown NRs on F-mica substrate. The NRs are detached from the substrate and picked up by PDMS film assisted by DI water. The PDMS film with NRs is then stamped on a glass slide, which is subsequently mounted on a 2D materials transfer stage (HQ Graphene) with targeting substrate with fabricated Au nanocones. Specific NR is aligned on Au cone arrays through an optical microscope and placed on top of them. Finally, the stage is heated to 65 °C to lift off the PDMS film, leaving the NR on Au nanocones.

TEPL measurement

Near-field optical measurements were carried out using a commercially available AFM system (OmegaScope; Horiba Scientific) coupled to a Raman spectrometer (LabRAM HR Evolution; Horiba Scientific). In this setup, a 594 nm laser was focused onto the tip of a gold coated AFM probe (AppNano Omni™ TERS-NC-Au) after passing through a long working distance microscope objective (100×, 0.7 NA) mounted at an angle (25° from horizontal). Enhanced PL from the sample was collected through the same objective. Spectra were taken with the tip in contact and also slightly retracted from the surface at each location. This allows for a pixel-wise subtraction of the far-field background, which was used to produce the TEPL maps shown in this work.

Low-temperature PL measurement

Low-temperature spectroscopy was conducted using a homebuilt confocal microscope. Light is focused on samples mounted in a Montana Instruments S50 cryostat using a Nikon Plan Fluor 40× long working distance objective. Excitation for MoS₂ was done with a 532 nm (Cobalt Samba™ 100) diode laser. Laser power on the sample was measured at 20 μW. The excitation source used for the WSe₂ spectra and $g^{(2)}(\tau)$ measurement was a 78 MHz pulsed supercontinuum laser (NKT Photonics SuperK EXTREME). An excitation wavelength of 532 nm was selected using an acoustic optical modulator and a tunable short-pass filter. The laser power on the sample was 60 nW. Integrated PL intensity was collected with a Micro Photon Devices (MPD) APD, and spectra were collected with a Horiba iHR320 spectrometer and a cooled Andor iDus CCD camera.

Data availability

The data that support the findings of this study are available from the corresponding authors upon request. Source data are provided with this paper.

References

- Giamarchi, T. *Quantum Physics in One Dimension* 1st edn, Vol. 442 (Oxford University Press, 2003).
- Huang, S. et al. Classical Coulomb blockade of a silicon nanowire dot. *Appl. Phys. Lett.* **92**, 213110 (2008).
- Niu, S. et al. Giant optical anisotropy in a quasi-one-dimensional crystal. *Nat. Photonics* **12**, 392–396 (2018).
- Noguchi, R. et al. A weak topological insulator state in quasi-one-dimensional bismuth iodide. *Nature* **566**, 518–522 (2019).
- Harutyunyan, A. R. Carbon nanotubes: helicity origin and envisioned applications. *Nano Today* **56**, 102248 (2024).
- Rizzo, D. J. et al. Topological band engineering of graphene nanoribbons. *Nature* **560**, 204–208 (2018).
- Kolmer, M. et al. Rational synthesis of atomically precise graphene nanoribbons directly on metal oxide surfaces. *Science* **369**, 571–575 (2020).
- Wang, H. S. et al. Towards chirality control of graphene nanoribbons embedded in hexagonal boron nitride. *Nat. Mater.* **20**, 202–207 (2021).
- Lyu, B. et al. Catalytic growth of ultralong graphene nanoribbons on insulating substrates. *Adv. Mater.* **34**, 2200956 (2022).
- Lyu, B. et al. Graphene nanoribbons grown in hBN stacks for high-performance electronics. *Nature* **628**, 758–764 (2024).
- Li, Y., Zhou, Z., Zhang, S. & Chen, Z. MoS₂ nanoribbons: high stability and unusual electronic and magnetic properties. *J. Am. Chem. Soc.* **130**, 16739–16744 (2008).
- Yue, Q. et al. Bandgap tuning in armchair MoS₂ nanoribbon. *J. Phys. Condens. Matter* **24**, 335501 (2012).
- Cai, Y., Zhang, G. & Zhang, Y.-W. Polarity-reversed robust carrier mobility in monolayer MoS₂ nanoribbons. *J. Am. Chem. Soc.* **136**, 6269–6275 (2014).
- Hu, T., Zhou, J., Dong, J. & Kawazoe, Y. Electronic and magnetic properties of armchair MoS₂ nanoribbons under both external strain and electric field, studied by first principles calculations. *J. Appl. Phys.* **116**, 064301 (2014).
- Ouyang, F. et al. Hydrogenation-induced edge magnetization in armchair MoS₂ nanoribbon and electric field effects. *Appl. Phys. Lett.* **104**, 071901 (2014).
- Balandin, A. A., Kargar, F., Salguero, T. T. & Lake, R. K. One-dimensional van der Waals quantum materials. *Mater. Today* **55**, 74–91 (2022).
- Chen, S. et al. Monolayer MoS₂ nanoribbon transistors fabricated by scanning probe lithography. *Nano Lett.* **19**, 2092–2098 (2019).
- Li, X. et al. Nickel particle-enabled width-controlled growth of bilayer molybdenum disulfide nanoribbons. *Sci. Adv.* **7**, abk1892 (2021).
- Deng, Y. et al. Lithography-free, high-density MoTe₂ nanoribbon arrays. *Mater. Today* **58**, 8–17 (2022).
- Li, S. et al. Vapour-liquid-solid growth of monolayer MoS₂ nanoribbons. *Nat. Mater.* **17**, 535–542 (2018).
- Chen, T. et al. Controlled growth of atomically thin MoSe₂ films and nanoribbons by chemical vapor deposition. *2D Mater.* **6**, 025002 (2019).
- Aljarb, A. et al. Ledge-directed epitaxy of continuously self-aligned single-crystalline nanoribbons of transition metal dichalcogenides. *Nat. Mater.* **19**, 1300–1306 (2020).
- Yang, P. et al. Epitaxial growth of inch-scale single-crystal transition metal dichalcogenides through the patching of unidirectionally orientated ribbons. *Nat. Commun.* **13**, 3238 (2022).
- Xue, G. et al. WS₂ ribbon arrays with defined chirality and coherent polarity. *Science* **384**, 1100–1104 (2024).
- Chowdhury, T. et al. Substrate-directed synthesis of MoS₂ nanocrystals with tunable dimensionality and optical properties. *Nat. Nanotechnol.* **15**, 29–34 (2020).
- Baker, R. T. K., Barber, M. A., Harris, P. S., Feates, F. S. & Waite, R. J. Nucleation and growth of carbon deposits from the nickel catalyzed decomposition of acetylene. *J. Catal.* **26**, 51–62 (1972).
- Dresselhaus, M. S., Dresselhaus, G., Sugihara, K., Spain, I. L. & Goldberg, H. A. In *Graphite Fibers and Filaments*. 12–34 (Springer Berlin Heidelberg, Berlin, Heidelberg, 1988).
- Harutyunyan, A. R. et al. Preferential growth of single-walled carbon nanotubes with metallic conductivity. *Science* **326**, 116–120 (2009).
- Givargizov, E. I. & Sheftal, N. N. Morphology of silicon whiskers grown by the VLS-technique. *J. Cryst. Growth* **9**, 326–329 (1971).
- Givargizov, E. I. Fundamental aspects of VLS growth. *J. Cryst. Growth* **31**, 20–30 (1975).
- Schubert, L. et al. Silicon nanowhiskers grown on <111> Si substrates by molecular-beam epitaxy. *Appl. Phys. Lett.* **84**, 4968–4970 (2004).
- Dubrovskii, V. G. et al. Diffusion-induced growth of GaAs nanowhiskers during molecular beam epitaxy: theory and experiment. *Phys. Rev. B* **71**, 205325 (2005).
- Kikkawa, J., Ohno, Y. & Takeda, S. Growth rate of silicon nanowires. *Appl. Phys. Lett.* **86**, 123109 (2005).
- Kodambaka, S., Tersoff, J., Reuter, M. C. & Ross, F. M. Diameter-independent kinetics in the vapor-liquid-solid growth of Si nanowires. *Phys. Rev. Lett.* **96**, 096105 (2006).
- Wu, Y. et al. Controlled growth and structures of molecular-scale silicon nanowires. *Nano Lett.* **4**, 433–436 (2004).
- Ji, Q. et al. Epitaxial monolayer MoS₂ on mica with novel photoluminescence. *Nano Lett.* **13**, 3870–3877 (2013).
- Li, X. et al. Surfactant-mediated growth and patterning of atomically thin transition metal dichalcogenides. *ACS Nano* **14**, 6570–6581 (2020).
- Shen, P.-C. et al. Ultralow contact resistance between semimetal and monolayer semiconductors. *Nature* **593**, 211–217 (2021).
- Liu, X. et al. The critical role of electrolyte gating on the hydrogen evolution performance of monolayer MoS₂. *Nano Lett.* **19**, 8118–8124 (2019).
- Harutyunyan, A. R. et al. Reduced carbon solubility in Fe nanoclusters and implications for the growth of single-walled carbon nanotubes. *Phys. Rev. Lett.* **100**, 195502 (2008).
- Kashchiev, D. In *Nucleation* 391–409 (Butterworth-Heinemann, Oxford, 2000).
- Jia, G. Y. et al. Excitonic quantum confinement modified optical conductivity of monolayer and few-layered MoS₂. *J. Mater. Chem. C* **4**, 8822–8828 (2016).
- Woggon, U. In *Optical Properties of Semiconductor Quantum Dots*. 43–101 (Springer Berlin Heidelberg, Berlin, Heidelberg, 1997).
- Wei, G. et al. Size-tunable lateral confinement in monolayer semiconductors. *Sci. Rep.* **7**, 3324 (2017).
- Bao, W. et al. Visualizing nanoscale excitonic relaxation properties of disordered edges and grain boundaries in monolayer molybdenum disulfide. *Nat. Commun.* **6**, 7993 (2015).
- Kastl, C. et al. The important role of water in growth of monolayer transition metal dichalcogenides. *2D Mater.* **4**, 021024 (2017).
- Branny, A., Kumar, S., Proux, R. & Gerardot, B. D. Deterministic strain-induced arrays of quantum emitters in a two-dimensional semiconductor. *Nat. Commun.* **8**, 15053 (2017).
- Azzam, S. I., Parto, K. & Moody, G. Prospects and challenges of quantum emitters in 2D materials. *Appl. Phys. Lett.* **118**, 240502 (2021).
- Darlington, T. P. et al. Imaging strain-localized excitons in nanoscale bubbles of monolayer WSe₂ at room temperature. *Nat. Nanotechnol.* **15**, 854–860 (2020).
- Yanev, E. S. et al. Programmable nanowrinkle-induced room-temperature exciton localization in monolayer WSe₂. *Nat. Commun.* **15**, 1543 (2024).

51. Chowdhury, T. et al. Anomalous room-temperature photoluminescence from nanostrained MoSe₂ monolayers. *ACS Photonics* **8**, 2220–2226 (2021).
 52. Peng, Z., Chen, X., Fan, Y., Srolovitz, D. J. & Lei, D. Strain engineering of 2D semiconductors and graphene: from strain fields to band-structure tuning and photonic applications. *Light Sci. Appl.* **9**, 190 (2020).
 53. Klein, J. et al. Engineering the luminescence and generation of individual defect emitters in atomically thin MoS₂. *ACS Photonics* **8**, 669–677 (2021).
 54. Thompson, A. P. et al. LAMMPS - a flexible simulation tool for particle-based materials modeling at the atomic, meso, and continuum scales. *Comput. Phys. Commun.* **271**, 108171 (2022).
 55. Takamoto, S. et al. Towards universal neural network potential for material discovery applicable to arbitrary combination of 45 elements. *Nat. Commun.* **13**, 2991 (2022).
 56. Martínez, L., Andrade, R., Birgin, E. G. & Martínez, J. M. PACKMOL: A package for building initial configurations for molecular dynamics simulations. *J. Comput. Chem.* **30**, 2157–2164 (2009).
 57. Stukowski, A. Visualization and analysis of atomistic simulation data with OVITO—the open visualization tool. *Model. Simul. Mater. Sci. Eng.* **18**, 015012 (2010).
 58. Nord, M., Vullum, P. E., MacLaren, I., Tybell, T. & Holmestad, R. Atomap: a new software tool for the automated analysis of atomic resolution images using two-dimensional Gaussian fitting. *Adv. Struct. Chem. Imaging* **3**, 9 (2017).
 59. O’Connell, E. N. et al. TopoTEM: A python package for quantifying and visualizing scanning transmission electron microscopy data of polar topologies. *Microsc. Microanal.* **28**, 1444–1452 (2022).
 60. Exarhos, A. L., Hopper, D. A., Grote, R. R., Alkauskas, A. & Bassett, L. C. Optical signatures of quantum emitters in suspended hexagonal boron nitride. *ACS Nano* **11**, 3328–3336 (2017).
- L.M.S. contributed to the NR synthesis. X.L. and Sh.W. developed NR transferring method. P.J.S., J.H., and A.R.H. initiated QE research. P.J.S. and N.B. planned the QE research. E.Y. and P.J.S. fabricated the nanocones and performed near-field measurements. S.W., J.S., M.S., and N.B. performed low-temperature QE property study. Q.-J.L. and J.L. performed the MD simulation. R.R.U. performed STEM imaging. Sh.W. performed AFM measurement. Y.S., Y.Z., and Y.Y. performed strain analysis. A.R.H. and X.L. drafted the manuscript. All the authors contributed to the analysis of data and writing the manuscript.

Competing interests

The authors declare no competing interests.

Additional information

Supplementary information The online version contains supplementary material available at <https://doi.org/10.1038/s41467-024-54413-9>.

Correspondence and requests for materials should be addressed to Avetik R. Harutyunyan.

Peer review information *Nature Communications* thanks Zhiwen Shi and the other, anonymous, reviewers for their contribution to the peer review of this work. A peer review file is available.

Reprints and permissions information is available at <http://www.nature.com/reprints>

Publisher’s note Springer Nature remains neutral with regard to jurisdictional claims in published maps and institutional affiliations.

Open Access This article is licensed under a Creative Commons Attribution-NonCommercial-NoDerivatives 4.0 International License, which permits any non-commercial use, sharing, distribution and reproduction in any medium or format, as long as you give appropriate credit to the original author(s) and the source, provide a link to the Creative Commons licence, and indicate if you modified the licensed material. You do not have permission under this licence to share adapted material derived from this article or parts of it. The images or other third party material in this article are included in the article’s Creative Commons licence, unless indicated otherwise in a credit line to the material. If material is not included in the article’s Creative Commons licence and your intended use is not permitted by statutory regulation or exceeds the permitted use, you will need to obtain permission directly from the copyright holder. To view a copy of this licence, visit <http://creativecommons.org/licenses/by-nc-nd/4.0/>.

© The Author(s) 2024

Acknowledgements

A.R.H. and X.L. thank Masahiko Izumi for supporting the research. A.R.H. thanks Ksenia V. Bets for illustration of growth. X.L. thanks Xinting Shuai for partially helping synthesis. The authors thank Dr. Baichang Li for electrical measurements. STEM characterization was conducted as part of a user project at the Center for Nanophase Materials Sciences, which is a US Department of Energy, Office of Science User Facility at Oak Ridge National Laboratory. AFM and AES measurements were performed at the Stanford Nano Shared Facilities (SNSF) RRID:SCR_023230, supported by the National Science Foundation under award ECCS-2026822.

Author contributions

A.R.H. conceptualized and designed research and suggested growth mechanism. A.R.H. and X.L. planned the experiments and studied the growth mechanism. X.L. developed the synthesis method. Sh.W. and